ACS APPLIED MATERIALS & INTERFACES

Research Article

Cite This: ACS Appl. Mater. Interfaces XXXX, XXX, XXX−XXX

www.acsami.org

Dictating Pt-Based Electrocatalyst Performance in Polymer Electrolyte Fuel Cells, from Formulation to Application

Tim Van Cleve,[†] Sunilkumar Khandavalli,[†] Anamika Chowdhury,[‡,§] Samantha Medina,[∥] Svitlana Pylypenko,[†,∥] Min Wang,[†] Karren L. More,[⊥] Nancy Kariuki,[#] Deborah J. Myers,[#] Adam Z. Weber,[‡] Scott A. Mauger,[†] Michael Ulsh,[†] and K. C. Neyerlin*[,†]

[†]Chemistry and Nanoscience Center, National Renewable Energy Laboratory, Golden, Colorado 80401, United States

[‡]Energy Conversion Group, Energy Technologies Area, Lawrence Berkeley National Laboratory, Berkeley, California 94720, United States

[§]Department of Chemical and Biomolecular Engineering, University of California, Berkeley, California 94720, United States

[∥]Colorado School of Mines, Golden, Colorado 80401, United States

[⊥]Oak Ridge National Laboratory, Oak Ridge, Tennessee 37830, United States

[#]Argonne National Laboratory, Lemont, Illinois 60439, United States

Supporting Information

ABSTRACT: In situ electrochemical diagnostics designed to probe ionomer interactions with platinum and carbon were applied to relate ionomer coverage and conformation, gleaned from anion adsorption data, with O_2 transport resistance for low-loaded (0.05 mg_{Pt} cm^{-2}) platinum-supported Vulcan carbon (Pt/Vu)-based electrodes in a polymer electrolyte fuel cell. Coupling the in situ diagnostic data with ex situ characterization of catalyst inks and electrode structures, the effect of ink composition is explained by both ink-level interactions that dictate the electrode microstructure during fabrication and the resulting local ionomer distribution near catalyst sites. Electrochemical techniques (CO displacement and ac impedance) show that catalyst inks with higher water content increase ionomer (sulfonate) interactions with Pt sites without significantly affecting ionomer coverage on the carbon support. Surprisingly, the higher anion adsorption is shown to have a minor impact on specific activity, while exhibiting a complex relationship with oxygen transport. Ex situ characterization of ionomer suspensions and catalyst/ionomer inks indicates that the lower ionomer coverage can be correlated with the formation of large ionomer aggregates and weaker ionomer/catalyst interactions in low-water content inks. These larger ionomer aggregates resulted in increased local oxygen transport resistance, namely, through the ionomer film, and reduced performance at high current density. In the water-rich inks, the ionomer aggregate size decreases, while stronger ionomer/Pt interactions are observed. The reduced ionomer aggregation improves transport resistance through the ionomer film, while the increased adsorption leads to the emergence of resistance at the ionomer/Pt interface. Overall, the high current density performance is shown to be a nonmonotonic function of ink water content, scaling with the local gas (H_2, O_2) transport resistance resulting from pore, thin film, and interfacial phenomena.

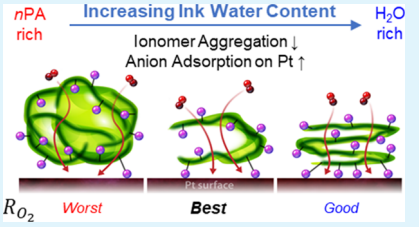

KEYWORDS: *Pt/C catalyst inks, ionomer coverage, ink formulation and processing, in situ electrochemical diagnostics, oxygen transport resistance*

INTRODUCTION

Polymer electrolyte fuel cells (PEFCs) are an attractive technology for mobile and stationary electric power generation which hold several benefits over conventional internal combustion engines, including higher efficiency and lower emissions. PEFCs convert the chemical energy stored in H_2 and O_2 into electrical energy, while producing only H_2O as the product. Despite their significant promise, commercially-available fuel cell vehicles currently utilize total areal platinum loadings greater than 0.3 mg_{Pt} cm^{-2},[1] exceeding both the US Department of Energy's (DOE) 2020 target of 0.125 g_{PGM} kW^{-1} at rated power (kW_{rated}, total areal loading of 0.125 mg_{Pt} cm^{-2}) and an industry-proposed stretch goal of 0.0625 g_{PGM} kW_{rated}^{-1},[2−4] which would require cathode loadings from 0.1 to 0.05 mg_{Pt} cm^{-2}, respectively.

To improve the overall PEFC performance and achieve these targets, research groups have applied various strategies,[5−7] from the incorporation of novel materials[8−12] to modified electrode fabrication methods[13−18] and conditioning protocols.[19−22] While advancements have been plentiful, both in scientific understanding and in PEFC performance, material improvements tend to be discussed relative to their targeted

Received: September 28, 2019
Accepted: November 19, 2019
Published: November 19, 2019

DOI: 10.1021/acsami.9b17614
ACS Appl. Mater. Interfaces XXXX, XXX, XXX−XXX

focus (e.g., oxygen reduction reaction mass activity of cathode catalysts), rather than their collective impact on electrode structure and performance.

The performance of PEFCs with low Pt loading has been shown to be impacted by ionomer chemistry,[23−25] Pt accessibility,[11,26,27] ionomer film thickness,[28−30] ionomer loading (I/C),[31−33] and other properties related to the local ionomer distribution and morphology in the catalyst layer. To that extent, recent studies have been able to visualize the ionomer distribution in membrane electrode assembly (MEA) cross sections using electron microscopy [scanning electron microscopy (SEM), transmission electron microscopy (TEM), scanning TEM (STEM), energy dispersive X-ray spectroscopy (EDS)] and X-ray tomography (nano-CT) techniques, with the purpose of examining the influence of process variables such as ionomer loading and the solvent ratio on the electrode microstructure. Orfanidi et al. observed that MEAs with smaller ionomer aggregate structures exhibited superior ORR and O_2-transport performance.[34] Lopez-Haro et al. utilized a series of high angle annual dark field (HAADF)/STEM images at different tilt angles and a tomographic reconstruction algorithm to produce 3D images of Nafion/carbon black layers, reporting an increase in ionomer coverage from 50 to 80% as the ionomer to carbon ratio was increased from 0.2 to 0.5 (by mass).[35,36] Cetinbas and co-workers utilized a combination of nano-CT and hybrid reconstruction techniques to refine the 3-D agglomerate microstructure and calculate ionomer film thickness distributions.[37,38] However, given the current resolution limitations, these techniques do not provide information on nanoscale phenomena such as ionomer adsorption or configuration, which has been hypothesized to impact ORR kinetics[39,40] and interfacial resistance at catalytic sites.[41−43]

Along these lines, ex situ characterization of catalyst inks has provided insight into the molecular interactions between the ionomer, solvent, and catalyst particles that govern the electrode structure. For example, Khandavalli et al. described how ionomer content impacts the stabilization of different catalyst/support aggregates, which is relevant for electrode fabrication,[44] and Berlinger et al. showed how the solvent ratio (and more specifically pH) affects ionomer's conformation in solution.[26,45]

While these studies are very insightful, a knowledge gap exists that would relate ionomer/catalyst, and/or ionomer/support, interactions with performance for as fabricated electrodes and validate any proposed structure−property relationships. This work aims to provide better resolution of the ionomer/catalyst interface by measuring Pt-sulfonate coverage and ionomer coverages on Pt and C surfaces utilizing in situ electrochemical diagnostics obtained on fully conditioned MEAs. Specifically, 50 wt % Pt/Vulcan (Pt/Vu) cathodes containing the Nafion 1000 EW ionomer prepared from different solvent (nPA: H_2O) ratios are investigated. While Pt/Vu is not a state-of-the-art material, its high Pt site accessibility (i.e., lack of particles buried in the carbon pores) makes it ideal for studying catalyst/ionomer interactions. Ionomer coverage and electrochemical performance trends are discussed along with supplemental characterization of MEAs and ink-level properties to elucidate the origins of the solvent effects observed here and elsewhere. While these studies are performed on PEFC electrodes, the effects and conclusions are relevant for other electrochemical systems (e.g., electrochemical CO_2 reduction, alkaline fuel cells, and electrolysis) and should facilitate future material (catalyst/ionomer) development and incorporation strategies.

EXPERIMENTAL METHODS

Fabrication of Catalyst-Coated Membranes. All catalyst inks were prepared using an established protocol.[16,22] Specifically, 50 wt % Pt/Vu (TKK, TEC10V50E) was dispersed in a mixture of deionized water (DI) and *n*-propanol (*n*-PA), resulting in a final concentration of 1.85 mg_{Pt} mL^{-1} solvent. Three different solvent ratios were investigated, such that the final Pt/Vu cathode inks were prepared with 24, 62, and 83 wt % water in solvent corresponding to the low-, moderate-, and high-water content inks, respectively, referenced throughout this study. The Dupont D2020 ionomer was then added to the ink solution to give the desired ionomer to carbon (I/C) mass ratio of 0.6.[31] Catalyst inks were dispersed with 20 s of horn sonication followed by 20 min of bath sonication in ice water.[16] The cathode catalyst layer was ultrasonically sprayed onto Nafion NR211 membranes (IonPower) using a Sono-Tek spray station with a 25 kHz accumist nozzle, targeting catalyst loadings of either 0.05 mg_{Pt} cm^{-2} (for 5 cm^2 testing), 0.10 mg_{Pt} cm^{-2} (for 50 cm^2 testing), or 0.30 mg_{Pt} cm^{-2} [for Electrochemical impedance spectroscopy (EIS) measurements]. Platinum loadings on individual electrodes were determined by X-ray fluorescence (XRF) (Fisher XDV-SDD). Anode electrodes were fabricated with Pt/HSC (TKK, TEC10E50E) dispersed in DI/*n*-PA (62 wt % water) with a 0.9 I/C and a 0.10 mg_{Pt} cm^{-2} loading.

Membrane Electrode Assembly - In Situ Electrochemical Diagnostics. Once fabricated, MEAs with cathode loadings of 0.10 and 0.30 mg_{Pt} cm^{-2} were tested using a 50 cm^2 double/triple (an/cath) serpentine flow field to acquire mass/specific activities, electrochemical surface area (ECSA), and ionomer coverage via CO displacement and EIS experiments. Catalyst-coated membranes (CCMs) with a cathode loading of 0.05 mg_{Pt} cm^{-2} were utilized in 5 cm^2 differential cells to obtain oxygen limiting current and the resulting oxygen transport resistances.[22,46,47] The CCMs were sandwiched between either (i) two 50 cm^2 SGL29 BC gas diffusion layers (GDLs), at 25% compression, or (ii) two 5 cm^2 Freudenberg H32C8 GDLs at 18% compression (more detail provided in Supporting Information). The CCMs, GDLs, and polytetrafluoroethylene gaskets were then placed between the flow fields and the bolts tightened to 40 in-pounds.

Break-In Procedures. The break-in procedures begin by heating the cell to 80 °C and holding the cell at an open circuit potential (load equivalent flow rates of 0.8/2.5 = H_2/air L_{std} min^{-1}), followed by a series of 5/10/5 voltage cycles in the fuel cell regime of 0.60−0.9 V for 4 min.[48]

Voltage Recovery. The voltage recovery (VR) step exposed the cell to 0.1 V under H2/air (950/500 sccm) for 2 h at 40 °C and 150% RH. This procedure was previously described[48] and shown to be a valuable step for the removal of sulfate, resulting in improved electrochemical performance across the entire potential range after the MEA had undergone significant degradation.[49]

H_2/O_2 Polarization Curves. The test protocol involved measuring the *I*−*V* curves from 0.4 V to OCV at 80 °C at 100 kPa O_2 partial pressure (150 kPa total pressure) and 100% RH for 4 min per point (average of last 1 min used) in the anodic direction. The ORR mass activities were reported at 0.90 V after applying high-frequency resistance (HFR) and hydrogen cross-over corrections.

H_2/Air Polarization Curves. The test protocol involved measuring the *I*−*V* curves from 0.3 V to OCV at 80 °C and at 150 kPa total pressure with 75% RH for 4 min per point (average of last 1 min used) in the anodic direction. Currents were only normalized by metal loading determined by XRF.

CO Displacement Chronoamperometry. The test protocol involved measuring the transient current response (*I*−*t*) resulting from the introduction of CO to an equilibrated electrode held at a constant potential.[32] During this process, adsorbed cationic/anionic species are displaced through oxidative/reductive process and the resulting displacement charge (q_{dis}) corresponds to the amount of charged surface species present at a specific potential. Experiments

DOI: 10.1021/acsami.9b17614
ACS Appl. Mater. Interfaces XXXX, XXX, XXX−XXX

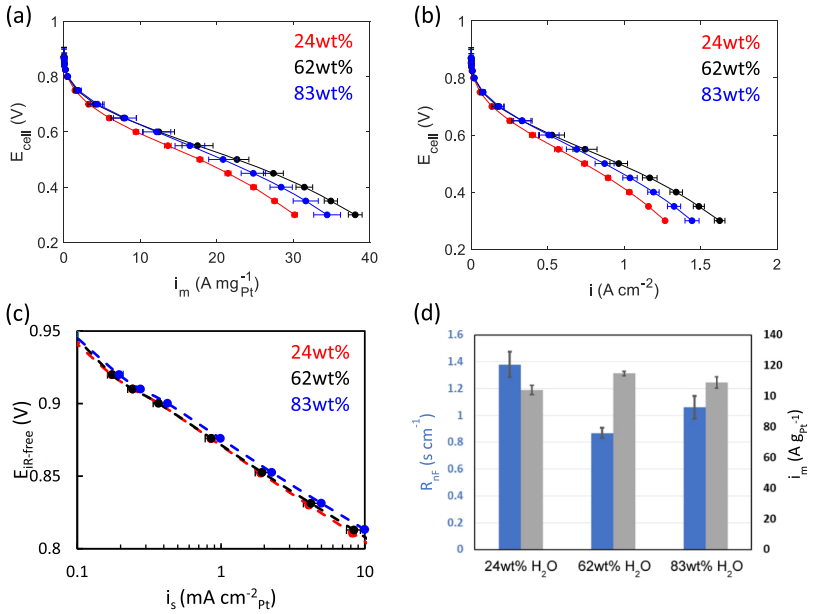

Figure 1. (a) Mass-based performance (i_m) and (b) nominal cell performance of fully conditioned Pt/Vu MEAs from 24 wt % (red), 62 wt % (black), and 83 wt % (blue) water ink formulations measured during air/H_2 polarization experiments at 150 kPa, 80 °C, and 75% RH. (c) Tafel plot comparing the specific activity of conditioned Pt/Vu MEAs from O_2/H_2 experiments at 150 kPa, 80 °C, and 100% RH. (d) Comparison of R_{nF} (determined at 80 °C and 75% RH) and mass activity at 0.9 $V_{iR\text{-}free}$ (H_2/O_2 150 kPa, 80 °C, and 100% RH) across Pt/Vu series. Error bars correspond to the standard deviation from experiments on at least three different MEAs.

were conducted at 80 °C and 75% RH, while the electrode was held at 0.1, 0.2, 0.3, 0.4 V, and 0.5 V_{cell}. Ionomer coverages were determined by normalizing the displacement charges measured at 0.3 V by CO stripping charge (Q_{CO}).

CO Stripping Voltammetry. Pt ECSA was determined by integrating the CO stripping charge (Q_{CO}) obtained from cyclic voltammetry (CV) immediately following CO displacement experiments. The cathode feed was purged with pure N_2 at 0.25 L_{std} min^{-1} prior to the first anodic sweep. CVs were performed immediately at 80 °C and 75% RH under H_2/N_2 sweeping from 0.05 to 0.9 V at 20 mV s^{-1}. The unit charge 420 μC cm^{-2} was assumed for CO integrated areas in determining the ECA.

O_2 Limiting Current Experiments. Limiting current measurements were performed at 80 °C and 75% RH, with 0.02, 0.03, and 0.05 mol fraction of oxygen. The limiting current was obtained at total cell pressures of 100, 150, 200, and 300 kPa. The limiting current was measured at constant voltages of 0.30, 0.24, 0.18, 0.12, and 0.06 V and held for 3 min. Because of the impact of hydrogen evolution on current densities obtained below 0.1 V, the maximum of the resulting current densities above 0.12 V was reported as the limiting current. Additional details on the procedure were previously described by Baker et al.[47]

H_2 and D_2 Limiting Current Experiments. Measurements were performed at 40 °C and 80% RH, with 1000 ppm H_2 or D_2 and 2% H_2 as the cathode and anode gases, respectively. Following several conditioning cycles between 0.08 and 0.095 V, steady state limiting current densities were measured at 0.3 V relative to the counter electrode and corrected for H_2 crossover. Additional details on the procedure were previously described by Spingler et al.[50,51]

Capacitance Coverage Experiments. EIS experiments were prepared on fully conditioned 50 cm^2 MEAs with 0.3 mg_{Pt} cm^{-2} using a Gamry Reference 3000 Potentiostat connected to a Gamry 30k Booster. EIS experiments were conducted at 80 °C with 1 atm pure H_2 and N_2 flowing at 100 cm^2 min^{-1} at anode and cathode gas lines, respectively. Experiments were run at 10, 25, 50, 75, and 100% RH with 30−60 min equilibration time before each measurement. EIS was measured 50 kHz−50 mHz at 0.45 and 0.2 V versus RHE with ±10 mV oscillations for CO-free and CO-doped experiments, respectively. Cathodes were exposed to 1% CO/N_2 feed for 15 min to allow for CO adsorption, then purged with pure N_2 prior to CO-doped experiments. Residual CO was oxidized after CO-doped EIS experiments and before CO-free EIS measurements.

MEA Characterization. *STEM/EDS Elemental Maps of CL Cross Sections.* EDS information was obtained by using a FEI Talos F200X electron microscope operating at 200 keV using the STEM mode. As-prepared and conditioned MEAs were embedded in Araldite 6005 epoxy resin mixture and cured at 60 °C for 16 h followed by trimming and ultramicrotomy using a 36° clearance angle Diatome diamond knife. The MEA cross sections were approximately 70 nm thick making them electron transparent for STEM, with both bright field (BF) and high angle annular dark field (HAADF) image production and EDS mapping of Pt, C, F, and S in the sample.

Ultrasmall Angle X-ray Scattering Experiments. The X-ray scattering data were collected on a combined Bonse−Hart (Ultrasmall angle X-ray scattering, USAXS) and pinhole (small angle and wide-angle X-ray scattering, SAXS/WAXS) instrument at beamline 9-ID-C at the Advanced Photon Source located at Argonne National Laboratory. Details regarding the optics and instrumentation have been previously reported.[52] The X-ray beam was monochromated via a pair of Si(220) crystals to an energy of 21 keV. The beam spot size for USAXS was 0.8 × 0.6 mm (horizontal × vertical) and 0.8 × 0.2 mm for SAXS. The X-ray beam exposure times for each sample were 90 s for USAXS and 30 s for SAXS. The samples were prepared by removing a section of the cathode catalyst layer from the membrane with single-sided, transparent Scotch tape using a press−peel technique. The samples were then supported in a custom-made sample holder for the SAXS/USAXS measurements. Patterns collected on a blank piece of tape were subtracted from the patterns acquired for the samples during data reduction. The data were corrected and reduced with NIKA software package,[53] and data analysis was conducted using IRENA software package.[54] Both packages were run on an IGOR Pro 7.0 (Wavemetrics). Particle size distribution was obtained from the measured scattering data using the maximum entropy (MaxEnt) method,[55] which involves a constrained optimization of parameters to solve the scattering equation

$$I(q) = |\Delta\varrho|^2 \int |F(q, r)|^2 (V(r))^2 N_p(r) dr_{int} \quad (1)$$

where, $I(q)$ is the scattered intensity, ϱ is the scattering length density of the particle, $F(q, r)$ is the scattering function at scattering vector q

DOI: 10.1021/acsami.9b17614
ACS Appl. Mater. Interfaces XXXX, XXX, XXX−XXX

of a particle of characteristic dimension r, V is the volume of the particle, and N_p is the number density of particles in the scattering volume.

Ink Characterization. *Dynamic Light Scattering and ζ-Potential Measurements.* Dynamic light scattering (DLS) and ζ-potential measurements were performed using a Zetasizer Nano ZS (Malvern Instruments Ltd, Malvern, U.K.). For the measurements, a high-concentration ζ cell (ZEN1010) was used, which allows measurements on more turbid samples such as carbon solutions and concentrated solutions.[56] These measurements were performed on relatively dilute inks compared to inks used for MEA fabrication at 0.1 wt % Pt/Vu as desired by the technique to avoid multiple scattering. The DLS measurements of ionomer solutions were carried out at 0.024 wt % using a disposable cuvette cell. The pH measurement of the ink dispersions was made using a pH meter (Thermo Fisher Scientific, Orion 4-Star) and is reported in Supporting Information. All measurements were performed at 25 °C. In the calculation of ζ-potential, the Helmholtz−Smoluchowski equation was used,[57] which assumes that the electric double-layer thickness is much smaller than the particle size, which is true here. At least five measurements were taken to ensure repeatability of the results.

RESULTS AND DISCUSSION

Ink Solvent Effects on MEA Performance. As prior works have shown,[16,23,26,34] despite rigorous control of catalyst loading, ionomer content, and operating conditions, slight changes in the ink formulation or processing can yield vastly different PEFC performances. Figure 1a,b compares the nominal and mass-based H_2/air performance of Pt/Vu CCMs with cathode catalyst layers prepared using inks with 24, 62, and 83% water (balance *n*PA). These three types of CCMs are termed 24%, 62%, and 83 wt % H_2O MEAs, respectively, in the remainder of the paper. At low current densities (higher cell voltages), minimal performance differences are observed. Tafel analysis of H_2/O_2 polarization based on Pt surface area (i.e., specific activity) clearly shows that the solvent ratio has little impact on ORR kinetics for this material set (Figure 1c). Regardless of their kinetic similarities, below 0.6 to 0.7 V, significant performance differences do emerge, where O_2 transport becomes limiting. Despite similar roughness factors (and ECA), the water-rich (62 and 83 wt % H_2O) MEAs exhibit significantly higher current densities at low operating voltages compared to the *n*PA-rich MEAs (24 wt % H_2O). However, this trend is not monotonic with ink water content in the catalyst ink because the 62 wt % H_2O MEAs outperformed the 83 wt % MEAs. Limiting current experiments corroborate these performance trends with the lowest non-Fickian O_2 transport resistance (R_{nF}) observed on moderate H_2O content MEAs, as shown in Figure 1d. Both the ionomer/catalyst interface and the total number of accessible active sites are key contributors to R_{nF}. Because all three Pt/Vu MEAs have equivalent ECAs (number of accessible sites, see Figure S1a), differences in R_{nF} likely arise from variations in the local ionomer/catalyst interface because of the increased ionomer thickness or alterations in ionomer orientation and/or confinement (i.e., the limitation in ionomer mobility due to the dominant interaction of ionomer chains tethered to a substrate).[23,28,58−62]

Characterization of Electrode Microstructures. Figure 2a−c (top) shows the select regions of 24, 62, and 83 wt % H_2O electrodes, respectively. Cross sections of as-prepared CCMs were characterized with STEM and EDS to determine whether alterations in ink formulation lead to observable differences in the ionomer distribution. For all MEAs, the catalyst layer/membrane interface is a region of higher Pt concentration. Figure 2a−c highlights the presence of the larger Pt/C agglomerates indicated by bright particles in the HAADF images and the representative pore structure near the top portion of the catalyst layers. Examining the elemental maps of the catalyst layer regions shown in Figure 2d−f (bottom), there are more concentrated regions with strong F signals for the electrodes fabricated using 24 and 83 wt % H_2O inks. This result would be indicative of thicker ionomer films or larger Pt/C ionomer aggregates in low and high-water content MEAs; however, when comparing the relative abundance of F (F/Pt) across the different sampling areas, there was as much variability between measurements on the same MEA (different regions) as across the solvent series. Because of the large heterogeneity throughout the catalyst layer, one must be careful of conclusions drawn from a single set of images and utilize other more robust techniques to probe the electrode structure and the resulting component interactions.

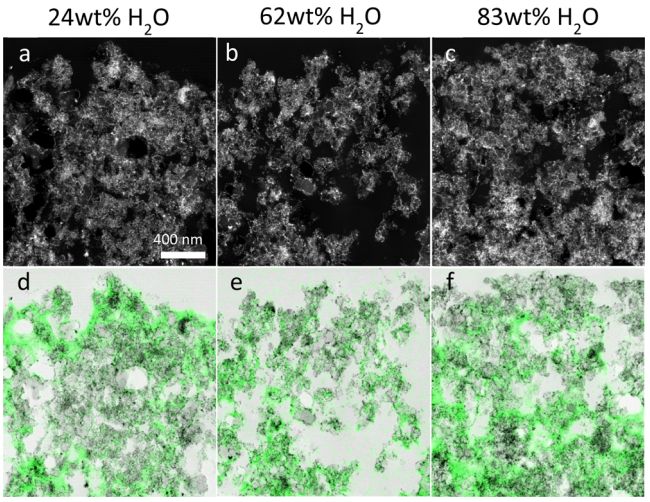

Figure 2. (a−c) HAADF images of the 24, 62, and 83 wt % H_2O catalyst layers. (d−f) High-magnification elemental maps of F (green) overlayed on the BF images, generated by STEM/EDS from MEA cross sections.

To obtain a global view of the electrode structure, the same set of as-prepared cathode catalyst layers were characterized using ultrasmall angle and small angle X-ray scattering (USAXS and SAXS, respectively) to determine the catalyst and carbon-ionomer particle, aggregate, and agglomerate size distributions. Unlike TEM, a local characterization techniques, USAXS and SAXS, provide the catalyst and carbon-ionomer size distributions over a larger area of ∼1 mm^2, the footprint of the X-ray beam. Figure 3 below illustrates that the carbon-ionomer agglomerate, aggregate, and Pt particle size distributions of electrodes made from the three different inks are nearly identical. Minor differences between the three CCLs are evident in the agglomerate and aggregate regions (low and intermediate Q ranges, respectively) of the scattering profiles. A log normal distribution fit to the intermediate Q region of the scattering profile shows that the volume average diameters of the carbon-ionomer aggregates for the 24, 62, and 83 wt % H_2O electrodes are 151 ± 2.3, 142 ± 2.3, and 151 ± 2.3 nm, respectively. While the statistically-significant larger aggregate size for the electrodes made from the low- and high-water content inks supports the observations noted above regarding the selected set of STEM/EDS images, presented in Figure 2,

DOI: 10.1021/acsami.9b17614
ACS Appl. Mater. Interfaces XXXX, XXX, XXX−XXX

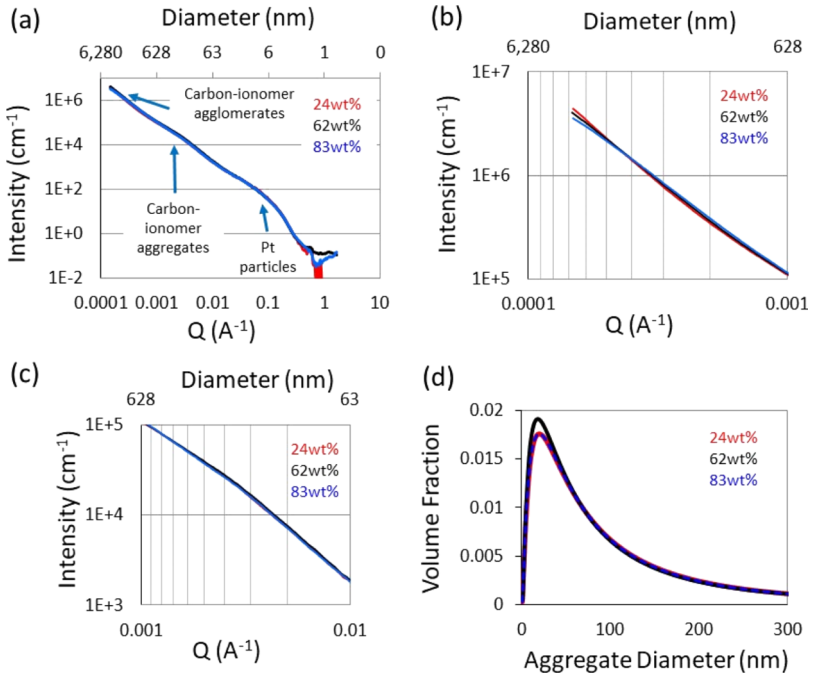

Figure 3. (a) USAXS/SAXS scattering profile, USAXS scattering profile in the (b) agglomerate region, (c) aggregate region, and (d) log normal aggregate size distribution.

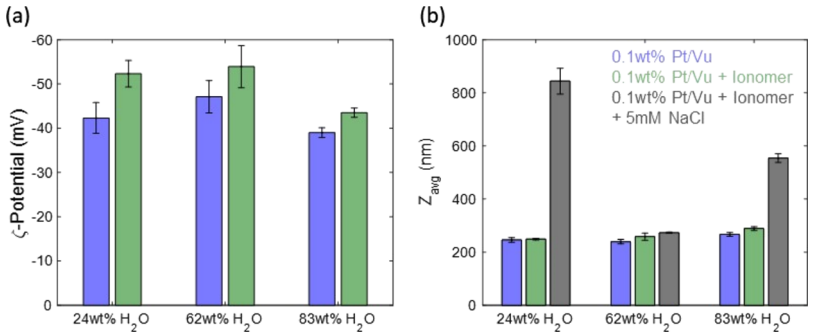

Figure 4. (a) ζ-potential and (b) Z_{avg} diameter for 0.1 wt % Pt/Vu catalyst inks [wt % = 100 × (Pt + Vu)/(Pt + Vu + solvent)] without ionomer (blue), with ionomer (green), and with 5 mM NaCl added (gray).

the location of the Pt particles on the exterior of the carbon support along with the modest difference in aggregate size should limit the contributions of performance and transport phenomena related to variations in aggregate size. This is a notably different scenario than what was recently identified for high-surface-area carbon-supported Pt.[63]

Further insight into the formulation−structure−performance relationships can be garnered by studying how solvent ratio is influencing the catalyst/ionomer interactions and impacting the electrode microstructure. The solvent ratio can significantly modify van der Waals, electrostatic, and solvation forces such as H-bonding, which govern the interparticle and ionomer/particle interactions that determine the ink microstructure.[64] Varying the ink water content modifies the dielectric constant of the solvent mixture, which was reported to be 27, 52, and 68 at 24 wt % H_2O, 58 wt % H_2O, and 82 wt % H_2O, respectively.[65] The medium dielectric constant influences both the van der Waal and the electrostatic interaction potential which are the two common interparticle interaction mechanisms that dictate the stability of colloidal particles which is often described by the Derjaguin−Landau−Verwey−Overbeek (DLVO) theory for aqueous colloidal dispersions.[66,67]

In Figure 4a, the ζ-potentials of the inks at different solvent ratios are presented to understand the relative electrostatic stability of Pt/Vu particles in different inks with and without the presence of ionomers. All cases have a large |ζ|-potential, indicating strong electrostatic repulsion, and as a result, there is little difference (<13%) in the average aggregate size (Z_{avg}) of the three inks, as measured by DLS (Figure 4b). The measured Z_{avg} is consistent with the carbon black primary aggregate size, indicating that the Pt/Vu particles are well dispersed.[68] The previous study by Khandavalli et al., however, observes a strong agglomeration in more concentrated ∼3 wt % Pt/Vulcan inks (which are at least 16× larger than the Pt/Vulcan wt % in this study) in similar solvent mixture containing 25 wt % H_2O.[44] The absence of agglomerates at all solvent ratios in the DLS measurements is likely due to the relatively dilute concentrations of the inks, where the agglomeration kinetics would be much slower at reduced particle concentrations.[69]

The addition of an ionomer slightly increases |ζ|-potential at all solvent ratios, indicative of better particle stability and enhanced interparticle repulsion following the adsorption of

DOI: 10.1021/acsami.9b17614
ACS Appl. Mater. Interfaces XXXX, XXX, XXX−XXX

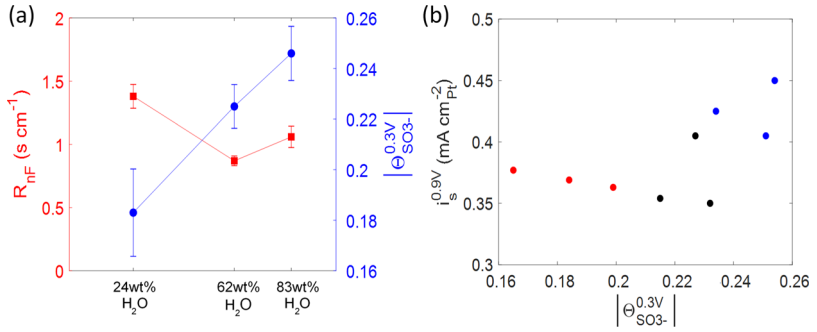

Figure 5. (a) Non-Fickian resistance (R_{nF}) and sulfonate coverage measured by CO displacement at 0.3 V_{cell} for different ink formulations. (b) Specific activity ($i_s^{0.9V}$) of fully conditioned MEAs 24 wt % (red), 62 wt % (black), and 83 wt % (blue) water MEAs measured at 0.9 V as a function of sulfonate coverage.

the ionomer. The addition of the ionomer also increases the Z_{avg} for the 62 and 83 wt % H_2O inks. Khandavalli et al. have shown a strong decrease in the agglomerated structure of more concentrated Pt/C inks with the addition of the ionomer using a combination of rheology and USAXS techniques.[44] However, such stabilization of Pt/Vu by the ionomer is not evident in Z_{avg} changes for all solvent ratios because the agglomeration is minimal, instead the Z_{avg} slightly increased (by ∼3−20 nm) because of the adsorbed ionomer on the particle surface, which increases the hydrodynamic size of the particle.

As the solvent ratio effect on the ink structure is not clearly evident, the stabilities of different inks were compared with the addition of salt (NaCl) that can induce some particle aggregation by screening the electrostatic interactions.[64] As shown in Figures S3a−d, the addition of salt reduces the |ζ|-potential and causes agglomeration, drastically increasing Z_{avg} in both 24 and 83 wt % water inks (see Figure 4b). Conversely, the most stable catalyst ink (i.e., highest |ζ|-potential), 62 wt %, had the smallest increase (<15 nm) in Z_{avg} following salt addition. Because electrostatic repulsion has been screened by the salt, it suggests the remaining stabilization is derived from steric stabilization of the adsorbed ionomer. This may indicate either a stronger association with Pt/Vu or a more expanded polymer structure at 62 wt % water than in the other solvent ratios.

In Situ Diagnostics to Determine Ionomer Coverage. To better resolve the differences in ionomer/catalyst interactions, in situ electrochemical techniques, specifically CO displacement chronoamperometry and EIS, were utilized to monitor the local coverage of ionomers on the catalyst as a function of ink formation. While a more detailed description of CO displacement chronoamperometry can be found in the Supporting Information and cited works,[32] such experiments performed at 0.3 V_{cell} directly measure the amount of sulfonate ions from the ionomer adsorbed on Pt sites. Figure 5a shows how SO_3^- coverage increases monotonically with ink water content. This observation is consistent with stronger ionomer/catalyst interactions present in water-rich inks and previous observations highlighting a more open (less dense) ionomer configuration, which increases with the solution dielectric constant, promoting the exposure of sulfonate groups.[45]

Surprisingly, SO_3^- coverage measured by CO displacement is not a good predictor for specific ORR activity. Figure 5b compares the specific activities ($i_s^{0.9V}$) at 0.9 $V_{iR\text{-}free}$ of fully conditioned MEAs with sulfonate coverages measured at 0.3 V ($\Theta_{SO_3^-}^{0.3V}$). For the small sample sizes investigated here, the 83 wt % H_2O MEAs exhibit slightly higher $i_s^{0.9V}$ despite 35−40% higher ionomer coverage compared to 24 wt % H_2O MEAs, which contradicts the conventional thinking that higher ionomer coverages should inhibit ORR turnover on Pt sites via a site-blocking mechanism.[70] Sulfate, bisulfate, and analogous sulfonic acid groups are well known poisons on Pt, capable of blocking multiple sites and greatly decreasing the ORR kinetics.[71−73] However, much of this previous work was conducted on polycrystalline Pt electrodes at low temperature in the presence of liquid water or under ultra-high vacuum conditions, which are drastically different from the operating conditions present in high-performance PEFCs. Here, all ink formulations exhibit similar Tafel behavior (with Tafel slopes ranging from 63 to 65 mV/decade) in the kinetic regime, further suggesting that ink formulation has limited the impact on observed ORR kinetics (see Figure 1c and Supporting Information).

Additionally, sulfonate coverages do not directly map with non-Fickian resistance (R_{nF}) values suggesting a more complex relationship between R_{nF} and sulfonate coverage or ionomer distribution. Because it is pressure insensitive, R_{nF} originates from limitations associated with Knudsen diffusion through small pores and thin films and interfacial barriers such as the Pt/ionomer interface at catalyst sites.[74,75] Figure 5a compares both non-Fickian resistance and sulfonate coverages on the set of fully conditioned MEAs. At 24 wt % H_2O, MEAs exhibit the lowest sulfonate coverage (0.18) but the highest R_{nF} (ca. 1.4 s cm^{-1}). As water content in the ink increases to 62 wt %, R_{nF} decreases while sulfonate coverage on Pt increases. Additional water content in catalyst ink leads to even higher sulfonate coverages because of the preferential ionomer configuration with more accessible sulfonate groups and higher R_{nF} for 83 wt % inks.[45] Mechanistically, the increased R_{nF} could result from increases in ionomer thickness and/or confinement.[26,76] However, the nonlinear trend between R_{nF} and sulfonate coverage suggests the Pt-sulfonate interactions alone do not determine O_2 transport barriers. A major limitation of the CO displacement technique is that it only measures sulfonate groups that directly interact with Pt sites, while neglecting hydrophobic backbone segments attached to Pt and C. The previous work suggests ionomer facilitates the break-up of large C agglomerates leading to better performance[16,44] but the DLS data, shown in Figure 4, refutes this claim as it relates to Pt/Vu-based inks, and the USAXS data, shown in Figure 3, shows that solvent composition had little effect on the agglomerate structure of the resulting electrodes. What remains unresolved is how the interactions between the ionomer with Pt and C dictate the electrode structure and the resulting electro-

DOI: 10.1021/acsami.9b17614
ACS Appl. Mater. Interfaces XXXX, XXX, XXX−XXX

chemical performance. Here, a previously described EIS technique was utilized to study such interactions.[77,78]

In general, this technique uses EIS to determine the relative coverage of ionomer and water on both Pt and C based on the double-layer capacitance (C_{dl}) of the electrode at several operating conditions, as depicted in Figure 6. Because

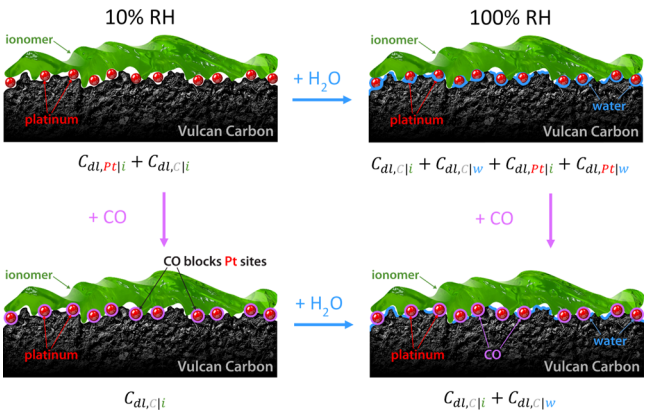

Figure 6. Depiction of the ionomer/catalyst interface under dry or wet conditions with and without CO present. Each condition has different interfaces contributing to double layer capacitance measured by EIS.

capacitance originates from material's ability to store energy as an electric dipole at the electrode interface, C_{dl} heavily depends on adsorption phenomena on Pt and C interfaces. Under dry conditions (10% RH), there is minimal H_2O adsorption, so all capacitance originates from the Ptlionomer and Clionomer interfaces. As RH increases, more water absorbs to both Pt and C surfaces increasing the total capacitance by introducing new Ptlwater and Clwater interfaces. The maximum capacitance is observed at 100% RH, and this value is used to normalize for the relative ionomer coverage obtained at 10% RH, as in eqs 2 and 3 below. In this model, specific capacitances for Pt and C interfaces are not required to determine the total interfacial area, rather the relative changes in C_{dl} with water adsorption are used to calculate ionomer coverage assuming only water and ionomer cover the surfaces, and capacitive contributions are proportional to coverage. Introduction of CO lowers the total electrode capacitance by effectively blocking Pt sites and, therefore, only measures charging on C surfaces. Figure 6 depicts the local adsorption phenomena present at each operating condition and summarizes which terms contribute to the measured capacitance.

$$\Theta_C = \frac{C_{dl,Cli}}{C_{dl,Cli} + C_{dl,Clw}} \quad (2)$$

$$\Theta_{Pt} = \frac{C_{dl,Pt|i}}{C_{dl,Pt|i} + C_{dl,Pt|w}} \quad (3)$$

Using the aforementioned EIS approach,[77] Figure 7 shows the ionomer coverages on Pt and carbon as a function of ink water content. Higher relative ionomer coverages are observed on C compared to Pt, which supports the hypothesis that ionomer is more critical for the stabilization of hydrophobic C support than of hydrophilic Pt sites. It is difficult to assert where there are significant differences in ionomer coverage on C because of high experimental uncertainty; though from this

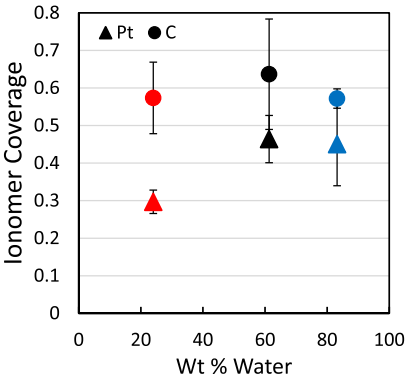

Figure 7. Ionomer coverage on carbon (circles) and Pt (triangles) determined by EIS for different ink formulations. Error bars correspond to the standard deviation from experiments on at least three different MEAs.

data, ionomer coverages on C and R_{nF} seem to have an inverse relationship, where the lower coverages lead to worse O_2 transport (Figure S8). What is abundantly clear, however, is that higher ionomer coverages on Pt are present in water-rich inks, consistent with the higher levels of sulfonate adsorption measured by CO displacement.

Because the nominal ionomer loading is constant, increasing surface coverage with higher ink water content implies higher interaction/association with Pt/Vu particles and a lower volume fraction of "free" ionomer aggregates throughout the electrode layer. Recently, Orfanidi et al. reported optimal higher current density performance for MEAs that were prepared in solvent ratios, which enable the smallest ionomer structures as measured by DLS and difficult to detect with SEM/EDS alone.[34] Figure 8 shows DLS particle size

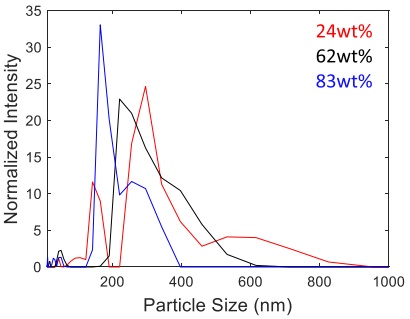

Figure 8. Particle-size distributions of dilute (0.024 wt %) ionomer dispersions in 24 wt % (red), 62 wt % (black), and 83 wt % (blue) water-content ink formulations characterized by DLS.

distributions of 0.024 wt % ionomer dispersions. Despite the constant shift to smaller aggregate sizes with increasing ink water content, we do not observe the same correlation between the ionomer size and MEA performance. Instead, what is observed is an optimum performance at 62 wt % water, where the sulfonate adsorption does not yet result in a confined ionomer structure, nor is the electrode subjected to transport through large aggregates of the ionomer. Deviations from the observations of Orfanidi et al. may result from the difference in catalyst (Pt/Vu vs Pt supported on graphitized Ketjen black) and ionomer (Nafion 1000EW versus low EW PFSA from Asahi Kasei) used in this study.

DOI: 10.1021/acsami.9b17614
ACS Appl. Mater. Interfaces XXXX, XXX, XXX−XXX

Compiling all the information from the studies presented here, Figure 9 depicts the effect of ink solvent ratio on the electrode microstructure, specifically the distribution of the ionomer within the catalyst layer. First and foremost, the USAXS data (Figure 3) indicate minimal difference in the break-up of carbon agglomerates to aggregates, and the DLS data (Figure 4b) indicate no significant difference in carbon aggregate size with ink water content. This is distinct from the ionomer behavior which exhibits water content-dependent PSDs. At low ink water content, ionomer exists as larger aggregates (Figure 8) that are loosely associated with catalyst particles because of lower surface coverage on Pt (Figures 4b, 5a, and 7). Increasing ink water content to 62 wt % results in slightly smaller ionomer aggregates (Figure 8), and more ionomer has been associated with Pt/Vu to help stabilize the particles (Figures 4b, 5a, and 7). At 83 wt % H_2O, the additional water leads to more ionomer (SO_3^-)/Pt interactions (Figure 5a) and more confined/compact ionomer thin films, which may increase R_{nF} (Figure 1d). While a clearer picture of the changes in ionomer distribution and the electrode structure is now evident at the microscale, local (nanoscale) or conformational changes in the ionomer structure can impact O_2 transport to Pt sites from a variety of mechanisms.

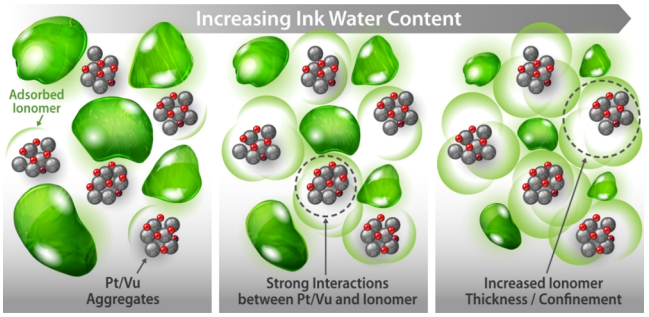

Figure 9. Electrode microstructure showing catalyst/ionomer interactions and relative ionomer aggregation at different ink solvent ratios. Ionomer is present in two states: "free" ionomer aggregate (large green shapes) and adsorbed ionomer, which strongly interacts with Pt/Vu aggregates. As ink water content increases, the "free" ionomer aggregates shrink as more of the ionomer interacts with Pt/Vu.

Interfacial Contributions to Gas Transport Resistance. To separate contributions from molecular weight (MW)-dependent and MW independent transport resistances and elucidate the relative contributions of pore (R_{pore}), ionomer film (R_{film}), and interfacial resistances (R_{int}) on gas transport in the catalyst layer, H_2 and D_2 limiting current experiments were also performed on Pt/Vu MEAs.[79] Similar to R_{nF} obtained via oxygen limiting the current described earlier (Figure 5a), Figure 10a shows gas transport resistances (R_{CL}) from both H_2 and D_2 were highest for 24 wt % H_2O and lowest for 62 wt % H_2O. In fact, there is excellent agreement among all the three limiting current experiments, where similar trends in gas transport resistance with changes in ink water content were observed (relative to 62 wt % H_2O-Figure S10).

However, because H_2 and D_2 have identical chemical properties and different masses, only molecular diffusion through pores and ionomer thin films will lead to difference in CL resistances, which are proportional to the ratio of square root of the mass ratio. Consequently, using eq 4, it is possible to calculate the fractional contribution of interfacial resistance to gas transport (f_{int}), where the remaining resistance is due to the molecular weight dependent transport resistance through pores and thin films ($R_{pore} + R_{film}$). This analysis finds only water rich (62 and 83 wt % H_2O) inks have significant contributions from interfacial resistance (34 ± 8 and 27 ± 8%, respectively), while the MEA prepared from the 24 wt % H_2O ink has negligible interfacial resistance. This is a significant finding, aligning both with the lower ionomer and sulfonate coverages previously obtained on the electrodes prepared from the 24 wt % H_2O ink.

$$f_{int} = 1 - \frac{\frac{R_{CL}^{D_2}}{R_{CL}^{H_2}} - 1}{\sqrt{\frac{MW_{D_2}}{MW_{H_2}}} - 1} \quad (4)$$

$$R_{int} = R_{H_2}^{CL} \times f_{int} \quad (5)$$

$$R_{pore} + R_{film} = R_{H_2}^{CL} \times (1 - f_{int}) \quad (6)$$

Using eqs 5 and 6, it is possible to compare the interfacial (R_{int}) and MW- dependent resistances ($R_{pore} + R_{film}$) across different MEAs. Comparing the MW-dependent ($R_{pore} + R_{film}$) and interfacial resistances (R_{int}) of H_2 shown in Figure 10b, it is clear Knudsen diffusion barriers through pores and/or thin ionomer films are present in all electrode structures.

Figure 11 illustrates the interplay between local oxygen transport resistance, ionomer and sulfonate coverage, and the nanoscale phenomena gleaned from H_2/D_2 experiments. When

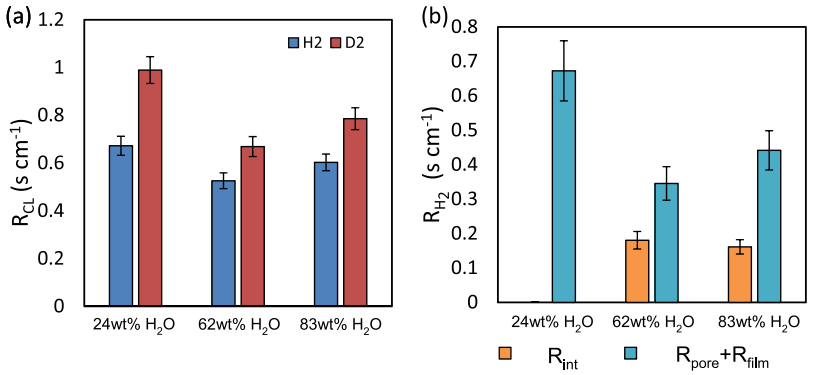

Figure 10. (a) Gas transport resistance in catalyst layer (R_{CL}) measured during H_2 (blue) and D_2 (red) limiting current experiments as a function of ink water content. (b) Portion of H_2 transport resistance from interfacial (R_{int}) and MW-dependent ($R_{pore} + R_{film}$) contributions.

DOI: 10.1021/acsami.9b17614
ACS Appl. Mater. Interfaces XXXX, XXX, XXX−XXX

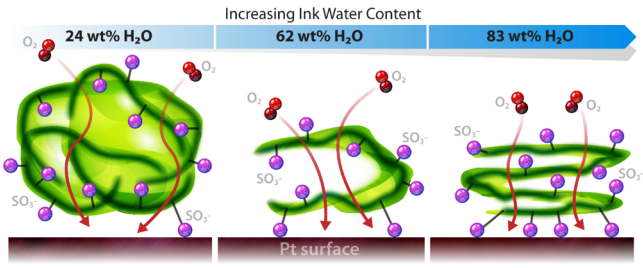

Figure 11. Proposed structure and orientation of ionomer/Pt interface leading to differences in O_2 transport across different Pt/Vu MEAs.

large ionomer aggregates are present and the hydrophobic backbone is exposed, as is the case for alcohol rich MEAs, the aggregates create thicker barriers adjacent to Pt sites, resulting in higher transport resistances despite minimal interfacial resistance because of weak ionomer/Pt interaction. On the other hand, when the sulfonate moieties are exposed to the surrounding solvent, sulfonate adsorption on Pt sites increases and leads to additional barriers caused by interfacial effects. However, the more open structure for both 62 and 83 wt % inks, gleaned earlier from ink-level experiments, leads to a reduction in the MW-dependent component (Figure 10b) and lowers overall transport rates relative to the 24 wt % ink.[45] In addition, as shown in Figure 10b, the increase in sulfonate adsorption from 62 to 83 wt % does not increase the interfacial resistance, but the MW-dependent transport contribution, suggesting thickening of the ionomer film and/or an increase in ionomer confinement.[26,61]

CONCLUSIONS

Insights from the ex situ characterization of catalyst inks comprised Nafion 1000 EW, 50 wt % Pt/Vu, and *n*-PA/H_2O, along with extensive in situ electrochemical testing of conditioned MEAs clearly demonstrates that ink water (alcohol) content has a significant impact on the distribution of the ionomer and its interaction with both Pt and C. CO displacement revealed a monotonic increase in anion (SO_3^-) adsorption with increasing ink water content because of changes in ionomer orientation. In water rich inks (62 and 83 wt %) the increase in sulfonate adsorption and ionomer orientation leads to the emergence of an interfacial resistance at the ionomer/Pt interface. Despite the onset of this additional resistance, the water rich inks resulted in electrodes with lower overall oxygen transport resistance because of both the decreasing size of ionomer aggregates and the changes in ionomer structure and distribution on Pt. Using H_2/D_2 limiting current measurements, this reduction in oxygen transport resistance, relative to electrodes prepared from the low water content (24 wt %) inks, was shown to correlate with a decrease in the molecular weight-dependent portion of local resistance derived from pores and thin ionomer films. Overall, high current density performance was shown to be a nonmonotonic function of ink water content, where 62 > 83 > 24 wt %, scaling predominantly with transport resistance through pores and thin films.

While the current study focuses only on the Nafion 1000 EW ionomer and Pt/Vu-based electrodes, future work aims to investigate the role of ionomer chemistry, ionomer loading, and electrocatalyst/carbon-support on electrode structure and performance. In general, similar trends are expected between solvent ratio and performance, where optimal formulations minimize ionomer aggregation without leading to substantial interfacial and/or film resistances. These results suggest future ionomer development, and incorporation should not solely focus on kinetic effects (weaker interactions between ionomer and electrocatalyst) but rather on how modifications to ionomer chemistry impacts ionomer confinement (densification) and the local distribution of ionomer on Pt and the resulting electrode microstructure, as these factors impact device-level performance, especially during operation at higher current densities.

ASSOCIATED CONTENT

Supporting Information

The Supporting Information is available free of charge at https://pubs.acs.org/doi/10.1021/acsami.9b17614.

MEA conditioning protocol, GDL compression calculation, ECA, mass activity, specific activity, and sulfonate coverage as a function of conditioning, ζ-potential, Z_{avg} diameter, and pH of inks with added salt, HAADF/STEM/EDS maps (Pt/F/C) of MEAs, CO displacements as a function of potential, Nyquist and $-1/\omega Z_{img}$ plots, C_{dl} of various interfaces, R_{nF} and ionomer coverage versus ink water content, DLS particles sizes (10−1000 nm), fractional contributions to R_{H_2}, changes in gas transport resistances, and list of symbols (PDF)

AUTHOR INFORMATION

Corresponding Author

*E-mail: kenneth.neyerlin@nrel.gov.

ORCID

Tim Van Cleve: 0000-0001-7233-5844
Sunilkumar Khandavalli: 0000-0003-3179-5718
Svitlana Pylypenko: 0000-0001-7982-734X
Min Wang: 0000-0002-5051-9199
Adam Z. Weber: 0000-0002-7749-1624
Scott A. Mauger: 0000-0003-2787-5029
K. C. Neyerlin: 0000-0002-6753-9698

Notes

The authors declare no competing financial interest.

ACKNOWLEDGMENTS

This work was authored in part by Alliance for Sustainable Energy, LLC, the manager and operator of the National Renewable Energy Laboratory for the U.S. Department of Energy (DOE) under contract no. DE-AC36-08GO28308. The submitted manuscript was also created, in part, by U Chicago Argonne, LLC, operator of Argonne National Laboratory, a DOE Office of Science laboratory, under contract DEAC02-06CH11357. Funding was provided by DOE Office of Energy Efficiency and Renewable Energy, Fuel Cell Technology Office, under the Fuel Cell Performance and Durability (FC-PAD) Consortium (contract DE-AC02-05CH11231 for LBNL), technology manager Greg Kleen and through the Fuel Cell Technology Office, technology manager Nancy Garland. Electron microscopy was conducted as a part of a user project at ORNL's Center for Nanophase Materials Sciences (CNMS), DOE Office of Science User Facility. X-ray scattering was performed at beamline 9-ID-C at the Advanced Photon Source (APS) at Argonne National Laboratory, a U.S. Department of Energy (DOE) Office of

DOI: 10.1021/acsami.9b17614
ACS Appl. Mater. Interfaces XXXX, XXX, XXX−XXX

Science User Facility, operated for the DOE Office of Science by Argonne National Laboratory under Contract DE-AC02 06CH11357. The Argonne authors thank Jan Ilavsky, Ivan Kuzmenko, and Matthew Firth of 9-ID-C. The authors are grateful for the continued collaborative and engaging discussions with Anu Kongkanand and many others from the GM fuel-cell activity program. The authors appreciate the frequent insightful discussions with Dr. Ahmet Kusoglu. The views expressed in the article do not necessarily represent the views of the DOE or the U.S. Government.

REFERENCES

(1) Borup, R. *FC-PAD: Fuel Cell Performance and Durability Consortium*; Annual Metric Review, 2017.
(2) Borup, R. *FC-PAD: Fuel Cell Performance and Durability Consortium*; Annual Merit Review, 2018.
(3) *Fuel Cell Multi-Year Research, Development and Demonstration Plan*, 2012.
(4) Kongkanand, A.; Mathias, M. F. The Priority and Challenge of High-Power Performance of Low-Platinum Proton-Exchange Membrane Fuel Cells. *J. Phys. Chem. Lett.* **2016**, *7*, 1127−1137.
(5) Litster, S.; McLean, G. PEM Fuel Cell Electrodes. *J. Power Sources* **2004**, *130*, 61−76.
(6) Shin, S.-J.; Lee, J.-K.; Ha, H.-Y.; Hong, S.-A.; Chun, H.-S.; Oh, I.-H. Effect of the Catalytic Ink Preparation Method on the Performance of Polymer Electrolyte Membrane Fuel Cells. *J. Power Sources* **2002**, *106*, 146−152.
(7) Mehta, V.; Cooper, J. S. Review and Analysis of PEM Fuel Cell Design and Manufacturing. *J. Power Sources* **2003**, *114*, 32−53.
(8) Alia, S. M.; Ngo, C.; Shulda, S.; Ha, M.-A.; Dameron, A. A.; Weker, J. N.; Neyerlin, K. C.; Kocha, S. S.; Pylypenko, S.; Pivovar, B. S. Exceptional Oxygen Reduction Reaction Activity and Durability of Platinum-Nickel Nanowires through Synthesis and Post-Treatment Optimization. *ACS Omega* **2017**, *2*, 1408−1418.
(9) Chen, C.; Kang, Y.; Huo, Z.; Zhu, Z.; Huang, W.; Xin, H. L.; Snyder, J. D.; Li, D.; Herron, J. A.; Mavrikakis, M.; Chi, M.; More, K. L.; Li, Y.; Markovic, N. M.; Somorjai, G. A.; Yang, P.; Stamenkovic, V. R. Highly Crystalline Multimetallic Nanoframes with Three-Dimensional Electrocatalytic Surfaces. *Science* **2014**, *343*, 1339−1343.
(10) Wang, X. X.; Hwang, S.; Pan, Y.-T.; Chen, K.; He, Y.; Karakalos, S.; Zhang, H.; Spendelow, J. S.; Su, D.; Wu, G. Ordered Pt_3Co Intermetallic Nanoparticles Derived from Metal−Organic Frameworks for Oxygen Reduction. *Nano Lett.* **2018**, *18*, 4163−4171.
(11) Yarlagadda, V.; Carpenter, M. K.; Moylan, T. E.; Kukreja, R. S.; Koestner, R.; Gu, W.; Thompson, L.; Kongkanand, A. Boosting Fuel Cell Performance with Accessible Carbon Mesopores. *ACS Energy Lett.* **2018**, *3*, 618−621.
(12) Lv, H.; Li, D.; Strmcnik, D.; Paulikas, A. P.; Markovic, N. M.; Stamenkovic, V. R. Recent Advances in the Design of Tailored Nanomaterials for Efficient Oxygen Reduction Reaction. *Nano Energy* **2016**, *29*, 149−165.
(13) Breitwieser, M.; Klingele, M.; Vierrath, S.; Zengerle, R.; Thiele, S. Tailoring the Membrane-Electrode Interface in PEM Fuel Cells: A Review and Perspective on Novel Engineering Approaches. *Adv. Energy Mater.* **2018**, *8*, 1701257.
(14) Brodt, M.; Wycisk, R.; Pintauro, P. N. Nanofiber Electrodes with Low Platinum Loading for High Power Hydrogen/Air PEM Fuel Cells. *J. Electrochem. Soc.* **2013**, *160*, F744−F749.
(15) Gulzow, E.; Kaz, T. New Results of PEFC Electrodes Produced by the DLR Dry Preparation Technique. *J. Power Sources* **2002**, *106*, 122−125.
(16) Wang, M.; et al. Impact of Catalyst Ink Dispersing Methodology on Fuel Cell Performance Using In-Situ X-ray Scattering. *ACS Appl. Energy Mater.* **2019**, *2*, 6417−6427.
(17) Kocha, S. *Best Practices and Benchmark Activities for ORR Measurements by the Rotating Disk Electrode Technique FC111*; Annual Metric Review, 2014.
(18) Ulsh, M.; Mauger, S. A. *Material-Process-Performance Relationships in PEM Catalyst Inks and Coated Layers*; Annual Metric Review, 2019.
(19) Debe, M. K. Nanostructured Thin Film Electrocatalysts for PEM Fuel Cells - A Tutorial on the Fundamental Characteristics and Practical Properties of NSTF Catalysts. *ECS Trans.* **2012**, *45*, 47−68.
(20) Debe, M. K. *Advanced Cathode Catalysts and Supports for PEM Fuel Cells*; Annual Metric Review, 2010.
(21) Kabir, S.; Bender, G.; Klein, W. E.; Kocha, S. S.; Neyerlin, K. C. Investigating the Effects of Catalyst Loading and MEA Conditioning on Commercial Pt/C and State-of-the-Art Pt-Alloy/C Performance in a PEMFC. *Meet. Abstr.* **2018**, *MA2018−01*, 1743.
(22) Kabir, S.; Myers, D. J.; Kariuki, N. N.; Park, J.; Wang, G.; Baker, A.; Macauley, N.; Mukundan, R.; More, K. L.; Neyerlin, K. C. Elucidating the Dynamic Nature of Fuel Cell Electrodes as a Function of Conditioning: An Ex-situ Materials Characterization and In-situ Electrochemical Diagnostic Study. *ACS Appl. Mater. Interfaces* **2019**, DOI: 10.1021/acsami.9b11365, recently accepted.
(23) Ono, Y.; Ohma, A.; Shinohara, K.; Fushinobu, K. Influence of Equivalent Weight of Ionomer on Local Oxygen Transport Resistance in Cathode Catalyst Layers. *J. Electrochem. Soc.* **2013**, *160*, F779−F787.
(24) Kodama, K.; Motobayashi, K.; Shinohara, A.; Hasegawa, N.; Kudo, K.; Jinnouchi, R.; Osawa, M.; Morimoto, Y. Effect of the Side-Chain Structure of Perfluoro-Sulfonic Acid Ionomers on the Oxygen Reduction Reaction on the Surface of Pt. *ACS Catal.* **2018**, *8*, 694−700.
(25) Kusoglu, A.; Dursch, T. J.; Weber, A. Z. Nanostructure/Swelling Relationships of Bulk and Thin-Film PFSA Ionomers. *Adv. Funct. Mater.* **2016**, *26*, 4961−4975.
(26) Takahashi, S.; Mashio, T.; Horibe, N.; Akizuki, K.; Ohma, A. Analysis of the Microstructure Formation Process and Its Influence on the Performance of Polymer Electrolyte Fuel-Cell Catalyst Layers. *ChemElectroChem* **2015**, *2*, 1560−1567.
(27) Park, Y.-C.; Tokiwa, H.; Kakinuma, K.; Watanabe, M.; Uchida, M. Effects of Carbon Supports on Pt Distribution, Ionomer Coverage and Cathode Performance for Polymer Electrolyte Fuel Cells. *J. Power Sources* **2016**, *315*, 179−191.
(28) Paul, D. K.; McCreery, R.; Karan, K. Proton Transport Property in Supported Nafion Nanothin Films by Electrochemical Impedance Spectroscopy. *J. Electrochem. Soc.* **2014**, *161*, F1395−F1402.
(29) Modestino, M. A.; Kusoglu, A.; Hexemer, A.; Weber, A. Z.; Segalman, R. A. Controlling Nafion Structure and Properties via Wetting Interactions. *Macromolecules* **2012**, *45*, 4681−4688.
(30) Kudo, K.; Jinnouchi, R.; Morimoto, Y. Humidity and Temperature Dependences of Oxygen Transport Resistance of Nafion Thin Film on Platinum Electrode. *Electrochim. Acta* **2016**, *209*, 682−690.
(31) Liu, Y.; Murphy, M. W.; Baker, D. R.; Gu, W.; Ji, C.; Jorne, J.; Gasteiger, H. A. Proton Conduction and Oxygen Reduction Kinetics in PEM Fuel Cell Cathodes: Effects of Ionomer-to-Carbon Ratio and Relative Humidity. *J. Electrochem. Soc.* **2009**, *156*, B970.
(32) Garrick, T. R.; Moylan, T. E.; Carpenter, M. K.; Kongkanand, A. Editors' Choice-Electrochemically Active Surface Area Measurement of Aged Pt Alloy Catalysts in PEM Fuel Cells by CO Stripping. *J. Electrochem. Soc.* **2017**, *164*, F55−F59.
(33) Malko, D.; Lopes, T.; Ticianelli, E. A.; Kucernak, A. A Catalyst Layer Optimisation Approach using Electrochemical Impedance Spectroscopy for PEM Fuel Cells Operated with Pyrolysed Transition Metal-N-C catalysts. *J. Power Sources* **2016**, *323*, 189−200.
(34) Orfanidi, A.; Rheinlander, P. J.; Schulte, N.; Gasteiger, H. A. Ink Solvent Dependence of the Ionomer Distribution in the Catalyst Layer of a PEMFC. *J. Electrochem. Soc.* **2018**, *165*, F1254−F1263.
(35) Lopez-Haro, M.; Guetaz, L.; Printemps, T.; Morin, A.; Escribano, S.; Jouneau, P.-H.; Bayle-Guillemaud, P.; Chandezon, F.; Gebel, G. Three-Dimensional Analysis of Nafion Layers in Fuel Cell Electrodes. *Nat. Commun.* **2014**, *5*, 5229.

DOI: 10.1021/acsami.9b17614
ACS Appl. Mater. Interfaces XXXX, XXX, XXX−XXX

(36) Guetaz, L.; Lopez-Haro, M.; Escribano, S.; Morin, A.; Gebel, G.; Cullen, D. A.; More, K. L.; Borup, R. L. Catalyst-Layer Ionomer Imaging of Fuel Cells. *ECS Trans.* **2015**, *69*, 455−464.
(37) Cetinbas, F. C.; Ahluwalia, R. K.; Kariuki, N. N.; Myers, D. J. Agglomerates in Polymer Electrolyte Fuel Cell Electrodes: Part II. Transport Characterization. *J. Electrochem. Soc.* **2018**, *165*, F1059−F1066.
(38) Cetinbas, F. C.; Ahluwalia, R. K. Agglomerates in Polymer Electrolyte Fuel Cell Electrodes: Part II. Transport Characterization. *J. Electrochem. Soc.* **2018**, *165*, F1059−F1066.
(39) Subbaraman, R.; Strmcnik, D.; Paulikas, A. P.; Stamenkovic, V. R.; Markovic, N. M. Oxygen Reduction Reaction at Three-Phase Interfaces. *ChemPhysChem* **2010**, *11*, 2825−2833.
(40) Shinozaki, K.; Zack, J. W.; Richards, R. M.; Pivovar, B. S.; Kocha, S. S. Oxygen Reduction Reaction Measurements on Platinum Electrocatalysts Utilizing Rotating Disk Electrode Technique. *J. Electrochem. Soc.* **2015**, *162*, F1384−F1396.
(41) Mashio, T.; Malek, K.; Eikerling, M.; Ohma, A.; Kanesaka, H.; Shinohara, K. Molecular Dynamics Study of Ionomer and Water Adsorption at Carbon Support Materials. *J. Phys. Chem. C* **2010**, *114*, 13739−13745.
(42) Kudo, K.; Jinnouchi, R.; Morimoto, Y. Humidity and Temperature Dependences of Oxygen Transport Resistance of Nafion Thin Film on Platinum Electrode. *Electrochim. Acta* **2016**, *209*, 682−690.
(43) Schuler, T.; Chowdhury, A.; Freiberg, A. T.; Sneed, B.; Spingler, F. B.; Tucker, M. C.; More, K. L.; Radke, C. J.; Weber, A. Z. Fuel-Cell Catalyst-Layer Resistance via Hydrogen Limiting-Current Measurements. *J. Electrochem. Soc.* **2019**, *166*, F3020−F3031.
(44) Khandavalli, S.; Park, J. H.; Kariuki, N. N.; Myers, D. J.; Stickel, J. J.; Hurst, K.; Neyerlin, K. C.; Ulsh, M.; Mauger, S. A. Rheological Investigation on the Microstructure of Fuel Cell Catalyst Inks. *ACS Appl. Mater. Interfaces* **2018**, *10*, 43610−43622.
(45) Berlinger, S. A.; McCloskey, B. D.; Weber, A. Z. Inherent Acidity of Perfluorosulfonic Acid Ionomer Dispersions and Implications for Ink Aggregation. *J. Phys. Chem. B* **2018**, *122*, 7790−7796.
(46) Makharia, R.; Mathias, M. F.; Baker, D. R. Measurement of Catalyst Layer Electrolyte Resistance in PEFCs Using Electrochemical Impedance Spectroscopy. *J. Electrochem. Soc.* **2005**, *152*, A970−A977.
(47) Baker, D. R.; Caulk, D. A.; Neyerlin, K. C.; Murphy, M. W. Measurement of Oxygen Transport Resistance in PEM Fuel Cells by Limiting Current Methods. *J. Electrochem. Soc.* **2009**, *156*, B991−B1003.
(48) Zhang, J.; Paine, L.; Nayar, A.; Makharia, R. Methods and Processes to Recover Voltage Loss of PEM Fuel Cell Stack. U.S. Patent 0,195,324 A1, August 11, 2011.
(49) Zhang, J.; Litteer, B. A.; Coms, F. D.; Makharia, R. Recoverable Performance Loss Due to Membrane Chemical Degradation in PEM Fuel Cells. *J. Electrochem. Soc.* **2012**, *159*, F287−F293.
(50) Spingler, F. B.; Phillips, A.; Schuler, T.; Tucker, M. C.; Weber, A. Z. Investigating Fuel-Cell Transport Limitations using Hydrogen Limiting Current. *Int. J. Hydrogen Energy* **2017**, *42*, 13960−13969.
(51) Schuler, T.; Chowdhury, A.; Freiberg, A. T.; Sneed, B.; Spingler, F. B.; Tucker, M. C.; More, K. L.; Radke, C. J.; Weber, A. Z. Fuel-Cell Catalyst-Layer Resistance via Hydrogen Limiting-Current Measurements. *J. Electrochem. Soc.* **2019**, *166*, F3020−F3031.
(52) Ilavsky, J.; Jemian, P. R.; Allen, A. J.; Zhang, F.; Levine, L. E.; Long, G. G. Ultra-small-angle X-ray scattering at the Advanced Photon Source. *J. Appl. Crystallogr.* **2009**, *42*, 469−479.
(53) Ilavsky, J. Nika: software for two-dimensional data reduction. *J. Appl. Crystallogr.* **2012**, *45*, 324−328.
(54) Ilavsky, J.; Jemian, P. R. Irena: tool suite for modeling and analysis of small-angle scattering. *J. Appl. Crystallogr.* **2009**, *42*, 347−353.
(55) Jemian, P. R.; Weertman, J. R.; Long, G. G.; Spal, R. D. Characterization of 9Cr-1MoVNb steel by anomalous Small-Angle X-ray scattering. *Acta Metall. Mater.* **1991**, *39*, 2477−2487.
(56) Kaszuba, M.; Corbett, J.; Watson, F. M.; Jones, A. High-Concentration Zeta Potential Measurements using Light-Scattering Techniques. *Philos. Trans. R. Soc., A* **2010**, *368*, 4439−4451.
(57) Hunter, R. J. *Zeta Potential in Colloid Science*; Academic Press, 1981; pp 59−124.
(58) Kusoglu, A.; Weber, A. Z. New Insights into Perfluorinated Sulfonic-Acid Ionomers. *Chem. Rev.* **2017**, *117*, 987−1104.
(59) Schalenbach, M.; Hoefner, T.; Paciok, P.; Carmo, M.; Lueke, W.; Stolten, D. Gas Permeation through Nafion. Part 1: Measurements. *J. Phys. Chem. C* **2015**, *119*, 25145−25155.
(60) Siroma, Z.; Kakitsubo, R.; Fujiwara, N.; Ioroi, T.; Yamazaki, S.-i.; Yasuda, K. Depression of proton conductivity in recast Nafion film measured on flat substrate. *J. Power Sources* **2009**, *189*, 994−998.
(61) Eastman, S. A.; Kim, S.; Page, K. A.; Rowe, B. W.; Kang, S.; Soles, C. L.; Yager, K. G. Effect of Confinement on Structure, Water Solubility, and Water Transport in Nafion Thin Films. *Macromolecules* **2012**, *45*, 7920.
(62) Paul, D. K.; Karan, K. Conductivity and Wettability Changes of Ultrathin Nafion Films Subjected to Thermal Annealing and Liquid Water Exposure. *J. Phys. Chem. C* **2014**, *118*, 1828−1835.
(63) Cetinbas, F. C.; Ahluwalia, R. K.; Kariuki, N. N.; De Andrade, V.; Myers, D. J. Effects of Porous Carbon Morphology, Agglomerate Structure and Relative Humidity on Local Oxygen Transport Resistance. *J. Electrochem. Soc.* **2020**, *167*, 013508.
(64) Israelachvili, J. N. *Intermolecular and Surface Forces*; Academic Press: CA, 2011.
(65) Sato, T.; Chiba, A.; Nozaki, R. Composition-Dependent Dynamical Structures of 1-Propanol-Water Mixtures Determined by Dynamical Dielectric Properties. *J. Chem. Phys.* **2000**, *113*, 9748−9758.
(66) Derjaguin, B.; Landau, L. Theory of the Stability of Lyophobic Colloids: The Interaction of Sol Particles Having an Electric Double Layer. *Acta Physicochem. URSS* **1941**, *14*, 633−662.
(67) Verwey, E. J. W.; Overbeek, J. T. G. *Theory of the Stability of Lyophobic Colloids: The Interaction of Sol Particles Having an Electric Double Layer*; Elsevier: Amsterdam, 1948; pp 135−182.
(68) Soboleva, T.; Zhao, X.; Malek, K.; Xie, Z.; Navessin, T.; Holdcroft, S. On the Micro-, Meso-, and Macroporous Structures of Polymer Electrolyte Membrane Fuel Cell Catalyst Layers. *ACS Appl. Mater. Interfaces* **2010**, *2*, 375−384.
(69) Mewis, J.; Wagner, N. *Colloidal Suspension Rheology*; Cambridge University Press: NY, 2012; pp 157−179.
(70) Markovic, N.; Gasteiger, H.; Ross, P. N. Kinetics of Oxygen Reduction on Pt(hkl) Electrodes: Implications for the Crystallite Size Effect with Supported Pt Electrocatalysts. *J. Electrochem. Soc.* **1997**, *144*, 1591−1597.
(71) Wang, H.; Macomber, C.; Christ, J.; Bender, G.; Pivovar, B.; Dinh, H. N. Evaluating the Influence of PEMFC System Contaminants on the Performance of Pt Catalyst via Cyclic Voltammetry. *Electrocatalysis* **2014**, *5*, 62−67.
(72) Christ, J. M.; Neyerlin, K. C.; Wang, H.; Richards, R.; Dinh, H. N. Impact of Polymer Electrolyte Membrane Degradation Products on Oxygen Reduction Reaction Activity for Platinum Electrocatalysts. *J. Electrochem. Soc.* **2014**, *161*, F1481−F1488.
(73) Christ, J. M.; Neyerlin, K. C.; Richards, R.; Dinh, H. N. Concentration Effects of Polymer Electrolyte Membrane Degradation Products on Oxygen Reduction Activity for Three Platinum Catalysts. *J. Electrochem. Soc.* **2014**, *161*, F1360−F1365.
(74) Owejan, J. P.; Owejan, J. E.; Gu, W. Impact of Platinum Loading and Catalyst Layer Structure on PEMFC Performance. *J. Electrochem. Soc.* **2013**, *160*, F824−F833.
(75) Greszler, T. A.; Caulk, D.; Sinha, P. The Impact of Platinum Loading on Oxygen Transport Resistance. *J. Electrochem. Soc.* **2012**, *159*, F831−F840.
(76) Page, K. A.; Kusoglu, A.; Stafford, C. M.; Kim, S.; Kline, R. J.; Weber, A. Z. Confinement-Driven Increase in Ionomer Thin-Film Modulus. *Nano Lett.* **2014**, *14*, 2299−2304.

DOI: 10.1021/acsami.9b17614
ACS Appl. Mater. Interfaces XXXX, XXX, XXX−XXX

(77) Iden, H.; Ohma, A. An In Situ Technique for Analyzing Ionomer Coverage in Catalyst Layers. *J. Electroanal. Chem.* **2013**, *693*, 34−41.
(78) Iden, H.; Mashio, T.; Ohma, A. Gas Transport Inside and Outside Carbon Supports of Catalyst Layers for PEM Fuel Cells. *J. Electroanal. Chem.* **2013**, *708*, 87−94.
(79) Chowdhury, A.; Radke, C. J.; Weber, A. Z. Transport Resistances in Fuel-Cell Catalyst Layers. *ECS Trans.* **2017**, *80*, 321−333.

DOI: 10.1021/acsami.9b17614
ACS Appl. Mater. Interfaces XXXX, XXX, XXX−XXX